



The $^{27}\text{Al}(p, \alpha)^{24}\text{Mg}$ reaction at astrophysical energies studied by means of the Trojan Horse Method applied to the $^2\text{H}(^{27}\text{Al}, \alpha^{24}\text{Mg})n$ reaction

S. Palmerini^{1,2,a} , M. La Cognata³, F. Hammache⁴, L. Acosta⁵, R. Alba³, V. Burjan⁶, E. Chávez⁵, S. Cherubini^{3,7}, A. Cvetinović⁸, G. D'Agata⁶, N. de Sérville⁴, A. Di Pietro³, P. Figuera³, Z. Fülöp⁹, K. Gaitán De Los Rios⁵, G. L. Guardo^{3,7}, M. Gulino^{3,10}, S. Hayakawa¹¹, G. G. Kiss⁹, M. La Commara^{12,13}, L. Lamia^{3,7}, C. Maiolino³, G. Manicó^{3,7}, C. Matei¹⁴, M. Mazzocco^{15,16}, J. Mrazek⁶, T. Parascandolo¹³, T. Petruse^{14,17}, D. Pierroutsakou¹³, R. G. Pizzone³, G. G. Rapisarda^{3,7}, S. Romano^{3,7}, D. Santonocito³, M. L. Sergi^{3,7}, R. Sparta^{3,7}, A. Tumino^{3,10}, H. Yamaguchi¹¹

¹ Dipartimento di Fisica e Geologia, Università degli Studi di Perugia, 06123 Perugia, Italy

² Istituto Nazionale di Fisica Nucleare, Sezione di Perugia, 06123 Perugia, Italy

³ Istituto Nazionale di Fisica Nucleare, Laboratori Nazionali del Sud, 95123 Catania, Italy

⁴ Institut de Physique Nucléaire d'Orsay, UMR8608, IN2P3-CNRS, Université Paris Sud 11, 91406 Orsay, France

⁵ Instituto de Física, Universidad Nacional Autónoma de México, A.P. 20-364, 01000 Mexico City, Mexico

⁶ Nuclear Physics Institute of the Czech Academy of Sciences, 250 68 Řež, Czech Republic

⁷ Dipartimento di Fisica e Astronomia "Ettore Majorana", Università degli Studi di Catania, 95123 Catania, Italy

⁸ Jozef Stefan Institute, Jamova cesta 39, Ljubljana, Slovenia

⁹ Institute for Nuclear Research (ATOMKI), P.O.B. 51, Debrecen 4001, Hungary

¹⁰ Facoltà di Ingegneria e Architettura, Università degli Studi "Kore", 94100 Enna, Italy

¹¹ Center for Nuclear Study, University of Tokyo, RIKEN Campus, Wako, Saitama 351-0198, Japan

¹² Dipartimento di Farmacia, Università degli Studi di Napoli "Federico II", 80131 Naples, Italy

¹³ Istituto Nazionale di Fisica Nucleare, Sezione di Napoli, 80126 Naples, Italy

¹⁴ Extreme Light Infrastructure - Nuclear Physics (ELI-NP)/Horia Hulubei National R&D Institute for Physics and Nuclear Engineering (IFIN-HH), Bucharest-Magurele, Romania

¹⁵ Dipartimento di Fisica e Astronomia, Università degli Studi di Padova, 35131 Padova, Italy

¹⁶ Istituto Nazionale di Fisica Nucleare, Sezione di Padova, 35131 Padova, Italy

¹⁷ Școala Doctorală de Inginerie și Aplicații Laserilor și Acceleratorilor, Politehnica University, Bucharest, Romania

Received: 12 January 2021 / Accepted: 12 August 2021

© The Author(s) 2021

Abstract The $^{27}\text{Al}(p, \alpha)^{24}\text{Mg}$ reaction, which drives the destruction of ^{27}Al and the production of ^{24}Mg in stellar hydrogen burning, has been investigated via the Trojan Horse Method (THM), by measuring the $^2\text{H}(^{27}\text{Al}, \alpha^{24}\text{Mg})n$ three-body reaction. The experiment covered a broad energy range ($E_{c.m.} \leq 1.5$ MeV), aiming to investigate those of interest for astrophysics. The results confirm the THM as a valuable technique for the experimental study of fusion reactions at very low energies and suggest the presence of a rich pattern of resonances in the energy region close to the Gamow window of stellar hydrogen burning (70–120 keV), with potential impact on astrophysics. To estimate such an impact a second

^a e-mail: sara.palmerini@pg.infn.it (corresponding author)

run of the experiment is needed, since the background due the three-body reaction hampered to collect enough data to resolve the resonant structures and extract the reaction rate.

1 Introduction

Aluminum has only one stable isotope, with $A = 27$, but in astrophysics it is the unstable isotope with $A = 26$ (and half-life 7.17×10^5 years) that arouses the greatest interest in the scientific community. The isotope is believed to provide the heat needed to differentiate the interiors of the small planetary bodies, but despite its importance in the formation of the rocky planets its stellar source is still debated. On the one side massive objects and supernova progenitors are the most likely candidates for this role, but the ^{26}Al fossil abundances would instead indicate that the main producers of Al-rich dust are low- and intermediate-mass stars during the asymptotic giant branch (AGB) phase [1–3].

A widely distributed γ emission at 1809 keV, following the isotope decay into excited states of ^{26}Mg , proves that ^{26}Al nucleosynthesis is active today in the Milky Way. The first clear detection of 1.808 MeV gamma lines from the bulge of the galaxy was made by the HEAO-3 satellite in 1984 [4], while the first mapping of the ^{26}Al emission in the Milky Way was due to the COMPTEL satellite [5]. Nowadays, modern millimeter and submillimeter interferometer arrays, as, e.g., ALMA (Atacama Large Millimeter/submillimeter Array) and NOEMA (Northern Extended Millimeter Array), are able to spatially identify discrete objects which are active sources of ^{26}Al in the Galaxy. However, only a few objects have been observed and they have not yet allowed to unambiguously identify the main galactic source of ^{26}Al . This is, for instance, the case of the detection of the molecule ^{26}AlF in the nova remnant CK Vul [6]. The observation itself is a great success of stellar spectroscopy, and the estimated abundance of ^{26}Al indicates that one of the merging objects was at least one solar-mass red giant star, but the red nova rate is too small to think that objects like CK Vul are the major producers of galactic ^{26}Al .

The fossil abundance of ^{26}Al is suggested by a superabundance of its daughter nucleus, ^{26}Mg , in comparison with the most abundant Mg isotope ($A = 24$) in meteorites. From the ratios of the abundances $^{26}\text{Mg}/^{24}\text{Mg}$ and $^{26}\text{Mg}/^{27}\text{Al}$ measured in presolar dust, meteorites and early solar system materials it is possible to estimate the $^{26}\text{Al}/^{27}\text{Al}$ ratio in the ancient Galaxy and to date these ancient solids [7]. For this reason, it is crucial to know with high precision the nucleosynthesis process not only of ^{26}Al but also of ^{27}Al and ^{24}Mg as well. In particular, all these nuclei take part to the so-called MgAl cycle, typical of high-temperature ($T = 0.055$ GK or $T_9 = 0.055$ in units of GK) H-burning of evolved stars (see [8] for an extensive discussion on the role of aluminum isotopes).

Because of the higher Coulomb barriers involved, the MgAl cycle is not as relevant as the CNO one for energy production in stars, but plays an important role in the nucleosynthesis of Al and Mg. In this framework, the $^{27}\text{Al}(p, \alpha)^{24}\text{Mg}$ reaction drives the destruction of ^{27}Al , the production of ^{24}Mg and closes the MgAl cycle when its rate exceeds the one of the competing $^{27}\text{Al}(p, \gamma)^{28}\text{Si}$ reaction. However, at temperatures $T_9 < 0.1$ it is difficult to compare the $^{27}\text{Al}(p, \alpha)^{24}\text{Mg}$ reaction with the competitor $^{27}\text{Al}(p, \gamma)^{28}\text{Si}$ channel because of the uncertainties, which are so large to make astrophysical predictions unreliable [8].

The most recent published rate for the $^{27}\text{Al}(p, \alpha)^{24}\text{Mg}$ reaction [9] is widely employed in astrophysical calculations, but at $T_9 \leq 0.1$ its lower, median and upper values are 1.85×10^{-11} , 4.34×10^{-11} and $8.51 \times 10^{-11} \text{ cm}^3 \text{ mol}^{-1} \text{ s}^{-1}$, respectively, spanning almost one order of magnitude. The uncertainty range becomes larger at lower temperatures. Such reaction rate is based on direct measurements data [10] (spanning only the low-energy region, between

200 and 360 keV, and setting upper limits for some resonance strengths), on spectroscopic data [11, 12], on transfer-reaction data [13] and on shell-model [14].

Nowadays, the abundances of magnesium isotopes in the interstellar medium are considered a powerful probe of star formation processes over cosmological timescales. This consideration is based on the assumption that the main contribution of ^{24}Mg comes from massive stars, whereas ^{25}Mg and ^{26}Mg come from intermediate mass objects [15], but this scenario could be modified, strengthened or weakened by more accurate measurements of proton capture reactions on Al and Mg isotopes in the energy range of stellar nucleosynthesis. For example, if the rate of the $^{27}\text{Al}(p, \alpha)^{24}\text{Mg}$ reaction were found to be higher at low temperatures, the production of ^{24}Mg could be more efficient even in intermediate mass objects (5–8 M_{\odot}).

Meteoritic grain abundances are among the most precise constraints available for nucleosynthesis studies because of their relatively small uncertainties, which in the case of magnesium and aluminum isotopic ratios are on average 10% and 15%, respectively.

However, in the last years, important information about Mg and Al nucleosynthesis is coming also from high-resolution stellar spectroscopy. It has shown that the already known anti-correlation of Mg-Al abundances of red-giant-branch stars of globular clusters (e.g., $\omega - \text{Cen}$, M4, NGC 2808) hides the existence of multiple stellar populations, and that, in some cases, the relative abundances of ^{24}Mg , ^{25}Mg and ^{26}Mg do not show any obvious correlation with Al abundances [16, 17]. To account for these observations a complicated scenario with various polluters (massive fast rotating stars, intermediate mass AGB and super AGB stars) is required [18], along with quite specific assumptions in the theoretical models, because in the narrow T_9 range between 0.07 and 0.08 the temperature of the stellar H-burning makes the difference among producing, saving or destroying ^{24}Mg [19]. Therefore, it is crucial to measure with high precision the $^{27}\text{Al}(p, \alpha)^{24}\text{Mg}$ reaction rate, as well as the rates of all the reactions involved in the MgAl cycle in the energy range typical of stellar nucleosynthesis.

Finally, it is worth noting that if resonances of the $^{27}\text{Al}(p, \alpha)^{24}\text{Mg}$ reaction will be found at low energies, also the contribution of low-mass-star H-burning to the Al nucleosynthesis should be revised.

2 Experimental method and setup

The $^{27}\text{Al}(p, \alpha)^{24}\text{Mg}$ reaction has been investigated using the Trojan Horse Method (hereafter THM), which is an experimental indirect technique already successfully applied to study several astrophysically relevant reactions by using appropriate three-body quasi-free (QF) processes [20, 21]. The method has proven to be particularly suited for acquiring information on charged particle-induced reaction cross sections at astrophysical energies, since it allows one to overcome the Coulomb barrier in the two-body entrance channel. In particular, many (p, α) reactions involved in low- and high-temperature H-burning networks have been measured, including a few involving radioactive nuclei (see, e.g., [22] and [23] and references therein for the $^{18}\text{F}(p, \alpha)^{15}\text{O}$) and neutrons (see, e.g., [24] for the $^{17}\text{O}(n, \alpha)^{14}\text{C}$, [25] for the $^7\text{Be}(n, \alpha)^4\text{He}$ and [26] for the $^3\text{He}(n, p)^3\text{H}$ reaction).

One can briefly describe the method as follows. A projectile a hits a target nucleus A , whose wave function has a large amplitude for a $s - b$ cluster configuration. Under proper kinematic conditions, the particle a interacts only with the part b (participant) of the target nucleus A , while the other part s behaves as a spectator to the process $a + b(+s) \rightarrow c + d(+s)$, which is a quasi-free (QF) mechanism. Since the bombarding energy is chosen to overcome the Coulomb barrier in the entrance channel for the $a + A \rightarrow c + d + s$ reaction, the particle

b can be brought into the nuclear field to induce the $a + b \rightarrow c + d$ reaction. Moreover, since the beam energy can be compensated for by the $b + s$ binding energy, the two-body reaction can take place at very low $a - b$ relative energy, e.g., in the region of astrophysical relevance.

We studied the $^{27}\text{Al}(p, \alpha)^{24}\text{Mg}$ reaction ($Q_2 = 1.6$ MeV) via the $^2\text{H}(^{27}\text{Al}, \alpha^{24}\text{Mg})n$ three-body reaction ($Q_3 = -0.6$ MeV). As it is shown in Fig. 1, the ^{27}Al is the projectile nucleus a impinging onto a deuteron (the target nucleus A), which acts as THM nucleus because of its obvious $p - n$ structure, being the neutron the spectator nucleus s .

To perform an experiment aimed to investigate the $^2\text{H}(^{27}\text{Al}, \alpha^{24}\text{Mg})n$ three-body reaction in the $^{27}\text{Al} - p$ energy range between the threshold and ~ 1.5 MeV, thus covering the region of astrophysical importance and a broad energy region where direct measurements are available for normalization, we used a 60 MeV ^{27}Al beam, delivered by the INFN-LNS Tandem (Catania, Italy), impinging onto a CD_2 target (isotopically enriched to 98%) $120 \mu\text{g}/\text{cm}^2$ thick, placed at 90° with respect to the beam axis. In this framework, the deuteron is an ultimate THM nucleus thanks to its $p - n$ structure, its low-binding energy ($B_{p-n} \sim 2.2$ MeV) and a very well-known $l = 0$ $p - n$ momentum distribution given in terms of the radial Hulthén wave function (see [27] for more details on the $p - n$ wave function).

In the plane wave impulse approximation, the three-body cross section can be expressed as:

$$\frac{d^3\sigma}{dE_\alpha d\Omega_\alpha d\Omega_{24Mg}} \propto (KF) |\Phi(p_n)|^2 \left(\frac{d\sigma}{d\Omega}\right)^{\text{HOES}} \quad (1)$$

where KF is a kinematical factor containing the final state phase space factor, $|\Phi(p_n)|^2$ is the momentum distribution of the spectator neutron inside the deuteron, and $\left(\frac{d\sigma}{d\Omega}\right)^{\text{HOES}}$ is the differential half-off-energy-shell (HOES) cross section for the two-body reaction $^{27}\text{Al}(p, \alpha)^{24}\text{Mg}$, the transferred proton being virtual (see, e.g., [28] and references therein for more details). The deduced two-body reaction cross section $\left(\frac{d\sigma}{d\Omega}\right)^{\text{HOES}}$ essentially represents the nuclear part alone, the Coulomb barrier being already overcome in the entrance channel, devoid of electron screening effects.

In the case of resonant reactions, a more advanced approach has been developed, to account for the HOES nature of the THM cross section and for the effect of energy resolution, both in the case of narrow [29,30] and broad resonances [31], firstly introduced by A.M. Mukhamedzhanov. Since the inspection of the resonance list in [9] shows that the low-energy cross section of the $^{27}\text{Al}(p, \alpha)^{24}\text{Mg}$ is dominated by narrow resonances, in comparison with the typical THM energy resolution of few ten of keV (FWHM), the application of the formalism thoroughly discussed in [29] will lead to the determination of the resonance

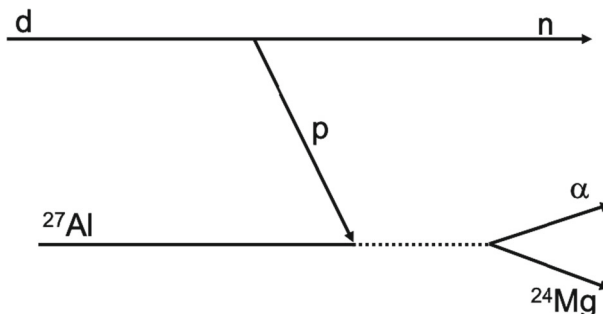


Fig. 1 Sketch of the QF transfer reaction to be selected among all the data recorded during the experiment

strengths from the THM cross section. A drawback of the method is the need to normalize the deduced resonance strengths to a reference one reported in the literature. However, it has been shown that extending the normalization procedure to more than one resonance greatly reduces possible systematic errors (see [32] for details).

In the case of emission of three particles in the reaction, only two of them have to be detected and identified. Indeed, measuring their energies and emission angles, the kinematic properties of the reaction are completely determined, so there is no need to use neutron detectors to observe the candidate spectator neutron. The experimental setup was optimized to detect the ejected α particle, that is, the lighter charged fragment, in coincidence with the ^{24}Mg recoil. Moreover, the detector positions were chosen to span the candidate $^2\text{H}(^{27}\text{Al}, \alpha^{24}\text{Mg})\text{n}$ QF kinematic region, whose occurrence is a necessary condition for the THM applicability.

Figure 2 shows a sketch of the experimental setup we adopted. It was symmetric with respect to the beam axis and consisted of two telescopes and two silicon position-sensitive detectors (PSD). Both telescopes covered an angular range from 4° to 8° on the left and on the right side of the beam axis. They were made up of an ionization chamber (IC) and a PSD to identify $Z = 12$ ions, in particular to discriminate between Mg and Al nuclei via the $\Delta E - E$ technique. The IC was filled with 65 mbar isobutane gas that provided an energy resolution of about 10%. A picture of the calibrated $\Delta E - E$ 2D spectrum for the IC1-PSD1 telescope is shown in Fig. 3, where the atomic number of the identified ions is marked. The red spot in the figure is linked to the ^{27}Al ions scattered off from carbon in the CD_2 targets. The other two silicon PSDs, used to detect the α particles in coincidence with ^{24}Mg , covered about 20° from 15° to 35° on the left and on the right of the beam line. The four 1000-micron PSDs had $50 \times 10 \text{ mm}^2$ sensitive area with 0.5 mm position resolution and an energy one of 0.5% (FWHM).

Energy and position calibration of the detectors spanning 15° – 35° was performed using the α particles from the $^6\text{Li}(^{12}\text{C}, \alpha)^{14}\text{N}$ reaction induced by a ^6Li beam at 8 MeV impinging on a CH_2 target. A standard three-peak alpha calibration source was also used for the low energy part of the α spectrum. The PSDs sitting at more forward angles and the ICs were calibrated by using scattering off Au and off ^{12}C of ^{24}Mg beams at 40, 45, 50 and 55 MeV.

3 Data analysis

Discrimination of Mg ions from other reaction and scattering products is the first step in the analysis, aiming at separating the reaction channel of interest, namely, the $^2\text{H}(^{27}\text{Al}, \alpha^{24}\text{Mg})\text{n}$

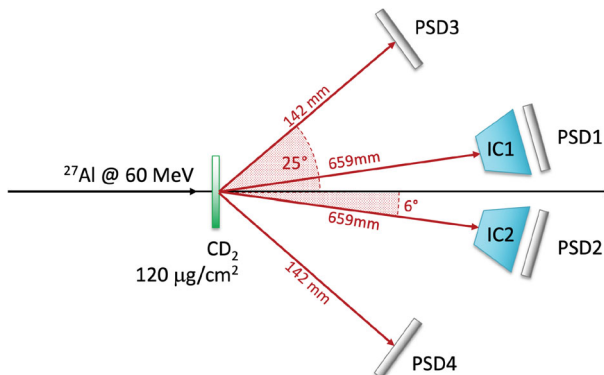
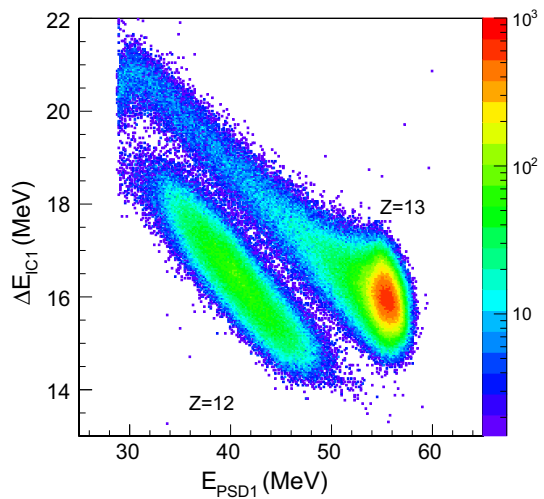


Fig. 2 Sketch of the experimental setup

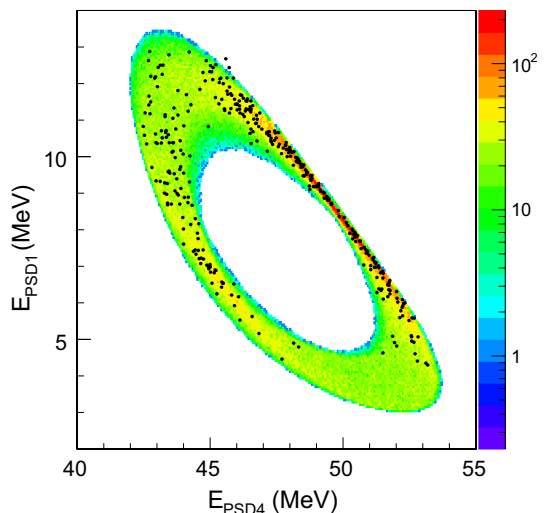
Fig. 3 2D $\Delta E - E$ spectrum for the telescope made up of the IC1 and the PSD1, detecting the energy loss and the residual energy of the impinging ions, respectively. The loci for Mg ($Z = 12$) and Al ($Z = 13$) isotopes can be easily identified thanks to their neat separation



three-body reaction, from other processes taking place in the target. From the analysis of reaction kinematics, it is apparent that the use of ICs as ΔE detectors did not introduce detection thresholds on the Mg energy spectra. Conversely, α particles energy spectra would have been significantly affected.

This is why we did not use ΔE to select α particles; however, this makes it necessary to investigate reaction kinematics to see if the implementation of coincident detection in PSD1–PSD4 and PSD2–PSD3, besides the selection of $Z = 12$ nuclei in the telescopes, is enough to suppress the contribution of background channels. To this purpose, for each angular couple $\theta_{\text{PSD1}} - \theta_{\text{PSD4}}$ and $\theta_{\text{PSD2}} - \theta_{\text{PSD3}}$ we have compared the experimental data with a Monte Carlo simulation accounting for reaction kinematics only. Indeed, events from the ${}^2\text{H}({}^{27}\text{Al}, \alpha {}^{24}\text{Mg})\text{n}$ three-body reaction should gather along characteristic loci in the $E_{\text{PSD1}} - E_{\text{PSD4}}$ and $E_{\text{PSD2}} - E_{\text{PSD3}}$ spectra. Figure 4 shows such comparison for the angular

Fig. 4 $E_{\text{PSD1}} - E_{\text{PSD4}}$ 2D spectrum for $4.1^\circ \leq \theta_{\text{PSD1}} \leq 5.1^\circ$ and $27^\circ \leq \theta_{\text{PSD4}} \leq 30^\circ$. THM data are shown in black, while the Monte Carlo simulated spectrum is shown in colors



condition $4.1^\circ \leq \theta_{\text{PSD1}} \leq 5.1^\circ$ and $27^\circ \leq \theta_{\text{PSD4}} \leq 30^\circ$, where the experimental THM data (in black), obtained just by gating on the $Z = 12$ locus in the $\Delta E - E$ spectrum, are juxtaposed to the simulated spectrum, obtained through the Monte Carlo code mentioned above. Similar results, in good agreement with the simulation, are obtained also for other angular couples and for the PSD2–PSD3 detectors couple. The inspection of the spectra makes it apparent that no background processes are populating the experimental spectra. This is also apparent from the experimental Q -value spectrum deduced from the THM reaction yield. It is shown in Fig. 5 as an histogram, while the calculated Q -value of the ${}^2\text{H}({}^{27}\text{Al}, \alpha {}^{24}\text{Mg})\text{n}$ reaction is shown as a vertical red line. Clearly, a single peak is present, excluding the occurrence of processes other than the ${}^2\text{H}({}^{27}\text{Al}, \alpha {}^{24}\text{Mg})\text{n}$ reaction of interest. The agreement with the theoretical Q -value is also a positive test of the accuracy of the energy and angular calibrations we performed.

4 Investigation of the QF mechanism

The THM formalism for the extraction of the resonance strengths requires the occurrence of the QF mechanism has been established, and the QF reaction yield separated from other reaction mechanisms. A first test is the study of the relative energy spectra to rule out the occurrence of the sequential decay processes. Indeed, the ${}^2\text{H}({}^{27}\text{Al}, \alpha {}^{24}\text{Mg})\text{n}$ three-body reaction might be described as a two-step process, where ${}^5\text{He}$ or ${}^{25}\text{Mg}$ is formed, later emitting a neutron to populate the $\alpha + {}^{24}\text{Mg} + \text{n}$ exit channel (the case of the formation of ${}^{28}\text{Si}$ as intermediate step will be considered later on). Indeed, if the neutron is emitted following the formation of an intermediate system, deuteron breakup cannot be direct and the ${}^2\text{H}({}^{27}\text{Al}, \alpha {}^{24}\text{Mg})\text{n}$ is not proceeding through a QF process.

To test this hypothesis, we have extracted the ${}^4\text{He}$ -n vs. ${}^{24}\text{Mg}$ -n relative energy spectrum, which is shown in Fig. 6. The occurrence of horizontal or vertical loci in the spectrum would signal the formation of ${}^5\text{He}$ or ${}^{25}\text{Mg}$ intermediate nuclei, respectively, since the sum

Fig. 5 THM reaction yield as a function of the calculated Q -value. The vertical red line points to the theoretical Q -value of the three-body ${}^2\text{H}({}^{27}\text{Al}, \alpha {}^{24}\text{Mg})\text{n}$ reaction ($Q_3 = -0.6238$ MeV)

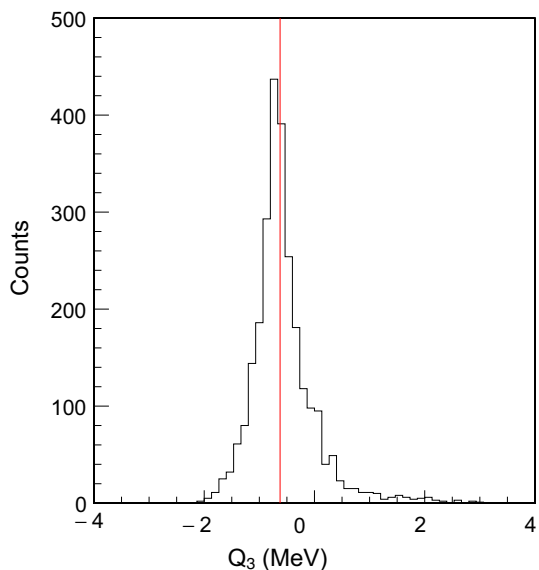
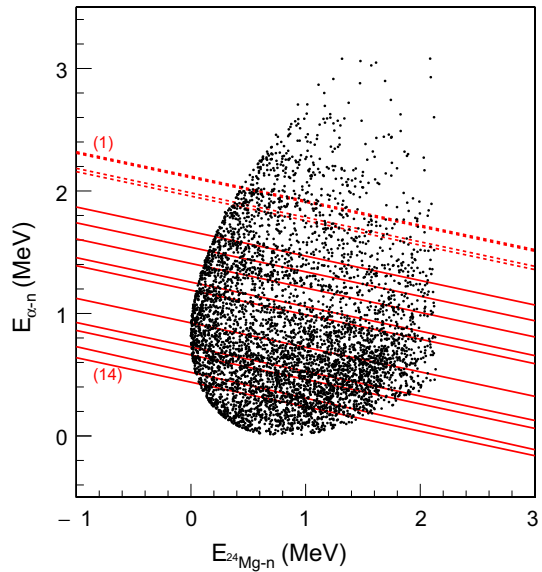


Fig. 6 $^4\text{He-n}$ versus $^{24}\text{Mg-n}$ relative energy 2D spectrum. It is obtained imposing only the $Z = 12$ condition on the $\Delta E - E$ spectrum. The red lines are the ^{28}Si levels listed in [9] with highest strength. Dashed lines are used for those states for which only upper limits to the resonant strengths could be set. The list of levels marked in the picture is given in Table 1



of the $^4\text{He-n}$ vs. $^{24}\text{Mg-n}$ relative energy with the corresponding neutron emission threshold equals the ^5He or ^{25}Mg excitation energies. Now, Fig. 6 clearly rules out the formation of such states above about $E_{\alpha-n} \sim 1$ MeV, no horizontal or vertical loci being observed in the experimental spectra. Conversely, sloping loci are observable and energy conservation consideration suggests to attribute them to the formation of ^{28}Si excited states. In particular, red lines are used to highlight the ^{28}Si states that are reported to have the highest strength for $^{27}\text{Al-p}$ relative energies less than about 1.5 MeV (dashed lines are used for states for which upper limits are available only). The list of levels marked in the figure is given in Table 1. Below about $E_{\alpha-n} \sim 1$ MeV, a cluster of events is present, which is not clearly attributable

Table 1 List of the levels showing the highest strength in the $^{27}\text{Al}(p, \alpha)^{24}\text{Mg}$ reaction below 1.6 MeV

	$E_{c.m.}$ (keV)	$\omega\gamma$ (eV)	$\delta\omega\gamma$ (eV)
(1)	71.5	$\leq 2.47 \times 10^{-14}$	–
(2)	84.3	$\leq 22.60 \times 10^{-13}$	–
(3)	193.5	$\leq 23.74 \times 10^{-7}$	–
(4)	214.7	$\leq 21.13 \times 10^{-7}$	–
(5)	486.74	0.11	0.05
(6)	609.49	0.275	0.069
(7)	705.08	0.52	0.13
(8)	855.85	0.83	0.21
(9)	903.54	4.3	0.4
(10)	1140.88	79	27
(11)	1316.7	137	47
(12)	1388.8	54	15
(13)	1519.4	12.5	2.5
(14)	1587.87	30.0	6.0

For resonances from (1) to (4) only upper limits are available. Resonance parameters (resonance energies, strengths and their uncertainties) are taken from [9]

to sequential processes due to the formation of ${}^5\text{He}$ or ${}^{25}\text{Mg}$ compound systems. Therefore, background might be expected at high $\alpha - {}^{24}\text{Mg}$ relative energies.

Since ${}^{28}\text{Si}$ states may be populated by direct (QF) or sequential process, further tests are necessary to establish if the ${}^2\text{H}({}^{27}\text{Al}, \alpha {}^{24}\text{Mg})n$ reaction proceeds through QF mechanism. A procedure that has turned out to be very effective is the extraction of the experimental neutron momentum distribution. Indeed, if the reaction mechanism is direct, the neutron momentum distribution should be the same as inside deuteron, the breakup process being adiabatic. Therefore, if the experimental momentum distribution follows the theoretical one, given by the squared deuteron wave function in momentum space [27], a necessary condition for the occurrence of the QF mechanism would be satisfied. From an experimental point of view, the neutron momentum distribution is obtained from the THM reaction yield by inverting Eq. 1, namely, dividing it by the kinematic factor under the assumption of a constant HOES cross section. This is obtained by selecting a narrow energy (and angular) cut, such that in this interval the variation is negligible. In the present case, this was accomplished by introducing a 100 keV wide energy cut around 2.75 MeV ${}^{24}\text{Mg} - \alpha$ relative energy. The resulting experimental neutron momentum distribution is shown in Fig. 7 as black solid circles, while the theoretical trend given by the squared Hulthén function in momentum space, as discussed in [27], is represented by a red line. The theoretical line was scaled to match the normalization of the experimental data. From this figure, it is apparent that below about $|p_s| \sim 50$ MeV/c, the agreement between the experimental and theoretical trend is very good, as it should be expected (see [28] for an extensive discussion). Similar results are obtained for other energy cuts. This makes us confident about the occurrence of the QF mechanism in the measured reaction and suggests the most suitable cut to introduce in the next steps to single out the QF yield.

5 Extraction of the $E_{c.m.}$ spectrum and final remarks

From the previous analysis, we will consider only events for which $|p_s| \leq 50$ MeV/c, the QF condition being satisfied and then Eq. 1 being applicable. Figure 8 shows the QF coincidence

Fig. 7 Solid symbols: experimental neutron momentum distribution obtained introducing, besides the data analysis cut, a 1.1 – 1.2 MeV gate on the ${}^{27}\text{Al}$ -p relative energy. The red line is the neutron momentum distribution in deuteron as in [27], normalized to the experimental data

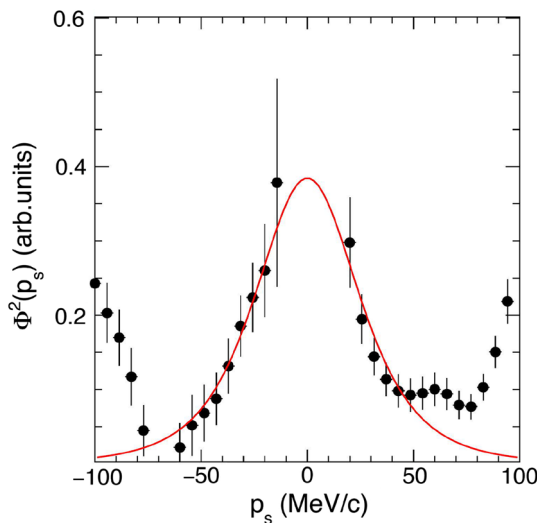
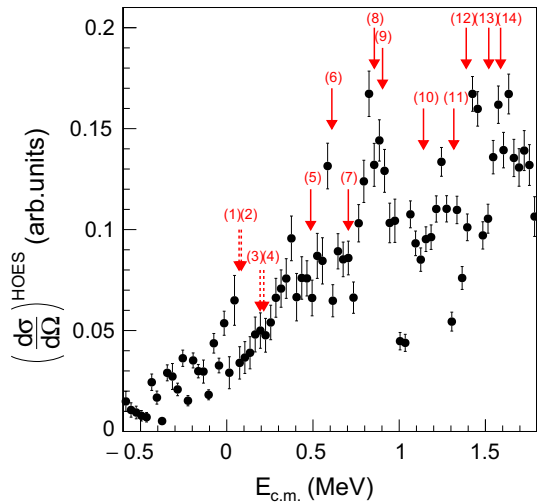


Fig. 8 HOES $^{27}\text{Al}(p, \alpha)^{24}\text{Mg}$ cross section $\left(\frac{d\sigma}{d\Omega}\right)^{\text{HOES}}$ as a function of $E_{c.m.}$. Arrows mark the states listed in Table 1. Dashed lines are used in the case only upper limits are available, as in Fig. 6. The spectrum was deduced taking $|p_s| \leq 50$ MeV/c



yield, projected on the $E_{c.m.}$ variable, calculated as follows:

$$E_{c.m.} = E_{^{24}\text{Mg}-\alpha} - Q_2 \quad (2)$$

where $E_{^{24}\text{Mg}-\alpha}$ is the $^{24}\text{Mg} - \alpha$ relative energy and Q_2 is the Q -value of the $^{27}\text{Al}(p, \alpha)^{24}\text{Mg}$ reaction [28]. The coincidence yield is divided by the product $(KF) |\Phi(p_s)|^2$ to obtain the HOES $^{27}\text{Al}(p, \alpha)^{24}\text{Mg}$ cross section $\left(\frac{d\sigma}{d\Omega}\right)^{\text{HOES}}$, that is, by inverting Eq. 1.

The obtained spectrum demonstrates the occurrence of a rich pattern of resonances (highlighted by the red arrows) among which four resonant states sit right at astrophysical energies (below ~ 0.2 MeV). These latter are indicated by dashed lines because only upper limits are available for them in the literature. In detail, several resonance groups are visible; starting from the high energy edge there is a peak linked to the population of resonances (12–14), with the state (12) probably well resolved from (13–14). Then, a peak due to states (10–11) and another strong peak for states (8–9) are visible, still populating energies above those of astrophysical interest. At lower energies, there is an excess of events with respect to a smooth background around ~ 0.5 MeV, probably linked to the population of states (5–7). Such bump is clearly seen even changing the energy bins. Focusing on the low energy region, the one mostly affecting astrophysical consideration, the situation is more ambiguous since an increase in the energy bin size would make the candidate peak at ~ 0 MeV disappear, so we cannot draw astrophysics considerations at present.

Indeed, if these resonance strengths (and of the one at 71.5 or at 84 keV in particular) were found greater than the established upper limit, the $^{27}\text{Al}(p, \alpha)^{24}\text{Mg}$ reaction rate would be larger than the (p, γ) competitor channel at astrophysical energy. The Gamow window of the $^{27}\text{Al}(p, \alpha)^{24}\text{Mg}$ reaction at the average temperature of stellar H-burning ($T_9 \sim 0.055$) ranges between 70 and 120 keV and the narrow temperature ranges between $T_9 = 0.07$ and 0.08, where the fate of ^{24}Mg nucleosynthesis in stars is decided, spans from 80 to 160 keV. Moreover, if the rate of the $^{27}\text{Al}(p, \alpha)^{24}\text{Mg}$ would be larger, the MgAl cycle will turn to be well closed with a larger production of ^{24}Mg and a more efficient destruction of ^{27}Al , even in low mass stars, and then the problem of the overproduction of ^{26}Al with respect to ^{27}Al in H-burning environments could be alleviated.

Unfortunately, owing to low statistics, it is not possible to extract angular distributions for each state. Indeed, binning of the coincidence yield limits the resolution, so several resonances often overlap. Therefore, we could not carry out angular integration, as discussed in [33]. Such integration is a pivotal step in the application of the procedure sketched in [29], to extract the resonance strengths from the peak areas. An especially important point to be addressed is the increase of $\left(\frac{d\sigma}{d\Omega}\right)^{\text{HOES}}$ with increasing $E_{\text{c.m.}}$, which is probably due to the unresolved contribution of the sequential decays pointed out when discussing Fig. 6.

In any case, this work has made it possible to establish the occurrence of the QF mechanism in the ${}^2\text{H}({}^{27}\text{Al}, \alpha{}^{24}\text{Mg})\text{n}$ reaction, which is a preliminary test for the application of the method. A future dedicated experiment with higher statistics would make it possible to explore the energy region below about 500 keV and determine the strengths of the observed levels at about 80 keV and at about 200 keV (see Table 1 for details). Also, the possibility to cover the energy region above about 500 keV where additional resonances are apparent, in particular around 900 keV (see Fig. 6), would make it possible to perform normalization of the resonant strengths as discussed in [32].

Acknowledgements The authors thank the LNS technical staff for the support during the experimental run. V. Burjan, J. Mrazek and G. D'Agata acknowledge the support from MEYS Czech Republic under the project EF16 013/0001679. G. G. Kiss acknowledges support from the NKFIH (NN128072), the UNKP-20-5-DE-2 New National Excellence Program of the Ministry of Human Capacities of Hungary and the Janos Bolyai research fellowship of the Hungarian Academy of Sciences. L. Acosta and E. Chávez acknowledge the support from DGAPA-UNAM IN107820, AG101120 and CONACyT 314857.

Funding Open access funding provided by Università degli Studi di Perugia within the CRUI-CARE Agreement.

Open Access This article is licensed under a Creative Commons Attribution 4.0 International License, which permits use, sharing, adaptation, distribution and reproduction in any medium or format, as long as you give appropriate credit to the original author(s) and the source, provide a link to the Creative Commons licence, and indicate if changes were made. The images or other third party material in this article are included in the article's Creative Commons licence, unless indicated otherwise in a credit line to the material. If material is not included in the article's Creative Commons licence and your intended use is not permitted by statutory regulation or exceeds the permitted use, you will need to obtain permission directly from the copyright holder. To view a copy of this licence, visit <http://creativecommons.org/licenses/by/4.0/>.

References

1. A.I. Karakas, C.J. Lattanzio, *PASA* **31**, 62 (2014)
2. P. Ventura et al., *Astrophys. J. Lett.* **83**, 17 (2016)
3. S. Palmerini et al., *Mon. Not. R. Astron. Soc.* **467**, 1193 (2017)
4. W.A. Mahoney, J.C. Ling, W.A. Wheaton, A.S. Jacobson, *Astrophys. J.* **286**, 578 (1984)
5. R. Diehl, C. Dupraz, K. Bennett, *Astron. Astrophys.* **298**, 445D (1995)
6. T. Kamiński, R. Tylanda, K.M. Menten et al., *Nat. Astron.* **2**, 778 (2018)
7. D. Vescovi et al., *Astrophys. J.* **863**, 115 (2018)
8. C. Iliadis, A.E. Champagne, A. Chieffi, M. Limongi, *Astrophys. J. Suppl. Ser.* **193**, 16 (2011)
9. C. Iliadis, R. Longland, A.E. Champagne, A. Coc, R. Fitzgerald, *Nucl. Phys. A* **841**, 31–250 (2010)
10. R. Timmermann et al., *Nucl. Phys. A* **477**, 105 (1988)
11. P.M. Endt, *Nucl. Phys. A* **521**, 1 (1990)
12. P.M. Endt, *Nucl. Phys. A* **633**, 1 (1998)
13. A.E. Champagne et al., *Nucl. Phys. A* **487**, 433 (1988)
14. P.M. Endt, J.G.L. Booten, *Nucl. Phys. A* **555**, 499 (1993)
15. E. Vangioni, A. Olive, *Mon Not R Astron Soc* **484**, 3561–3572 (2019)
16. K. Lind et al., *Astron. Astrophys.* **575**, L12 (2015)
17. G.S. Da Costa, J.E. Norris, D. Yong, *Astrophys. J.* **769**, 8 (2013)

18. E. Carretta, A. Bragaglia, S. Lucatello, R.G. Gratton, V. D'Orazi, A. Sollima, *Astron. Astrophys.* **615**, 17 (2018)
19. D. Yong, F. Grundahl, D.L. Lambert et al., *Astron. Astrophys.* **402**, 985 (2003)
20. R. Tribble et al., *Rep. Progr. Phys.* **77**, 106901 (2014)
21. C. Spitaleri et al., *Eur. Phys. J. A* **55**, 161 (2019)
22. M. La Cognata et al., *Astrophys. J.* **846**, 65 (2017)
23. S. Cherubini et al., *Phys. Rev. C* **92**, 5805 (2015)
24. G.L. Guardo et al., *Phys. Rev. C* **95**, 5807 (2017)
25. L. Lamia et al., *Astrophys. J.* **879**, 23 (2019)
26. R.G. Pizzone et al., *Eur. Phys. J. A* **56**, 199 (2020)
27. L. Lamia et al., *Phys. Rev. C* **85**, 025805 (2012)
28. C. Spitaleri et al., *Eur. Phys. J. A* **55**, 161 (2019)
29. M. La Cognata et al., *Astrophys. J.* **708**, 796 (2010)
30. A. Tumino et al., *Nature* **557**, 687 (2018)
31. M. La Cognata et al., *Astrophys. J.* **723**, 1512 (2010)
32. M. La Cognata et al., *Astrophys. J.* **805**, 128 (2015)
33. I. Indelicato et al., *Astrophys. J.* **845**, 19 (2017)